Screening effects on the electronic structure of the hydrogen molecular ion

Andrés Felipe Ordóñez-Lasso,[1,*] Fernando Martín,[1,2,3] and José Luis Sanz-Vicario[4,†]
[1]*Departamento de Química, Módulo-13, Universidad Autónoma de Madrid, 28049 Madrid, Spain*
[2]*Condensed Matter Physics Center (IFIMAC), Universidad Autónoma de Madrid, 28049 Madrid, Spain*
[3]*Instituto Madrileño de Estudios Avanzados en Nanociencia (IMDEA-Nano), Cantoblanco, 28049 Madrid, Spain*
[4]*Grupo de Física Atómica y Molecular, Instituto de Física, Universidad de Antioquia, Medellín, Colombia*
(Received 28 September 2016; published 20 January 2017)

We study the effect that a statically screened Coulomb potential represented by a Debye-Hückel-Yukawa potential has in the electronic structure of the simplest molecule H_2^+ within the Born-Oppenheimer approximation. The method of solution is based on a two-center partial-wave expansion expressed in confocal elliptic coordinates using B-spline polynomials. General algorithms for the computation of energies, wave functions, and dipole and nonadiabatic radial matrix elements are given in detail. As it occurs in atoms, screening in simple molecules shifts the energies of bound states upwards so that, as screening increases, every bound state eventually crosses the upper ionization threshold at a critical screening value. The loss of long-range Coulomb interactions has its effect in the structure of wave functions, and consequently in the dipole and nonadiabatic matrix elements at intermediate and long internuclear distances, which determine the dynamics in external electromagnetic fields and collisional processes. Other issues related to a practical solution of the arbitrary sign problem, as well as the assignment of angular and radial nodes to the variational eigenfunctions, and the appearance of molecular shape resonances and Borromean states in H_2^+ as screening increases, are also addressed in this work.

DOI: 10.1103/PhysRevA.95.012504

I. INTRODUCTION

Electrostatic screening plays a fundamental role in the description of plasmas, the structure of many-electron atoms and molecules, metals, and semiconductors in solid state physics, and electrochemistry in general. In atoms and molecules, the shielding of the long-range Coulomb force gives rise to effects such as pressure ionization (continuum lowering) and the removal of energy degeneracies. Screening at its most simple modelization can be described using the Debye-Hückel approximation [1] which amounts to replace the Coulomb potential by Yukawa-type potentials ($V = q_i q_j e^{-\lambda r_{ij}}/r_{ij}$) for each pair of charged particles $\{q_i, q_j\}$ separated by a distance r_{ij}. Here, λ denotes the screening parameter which, for instance, in the case of weakly coupled plasmas, can be expressed in terms of the density and temperature of the plasma [2]. Weak screening mostly affects the long-range part of the interacting potential, so that highly excited states are more affected than compact bound states. Strong screening, on the other hand, can prevent the formation of bound states entirely.

Because of the importance of charge interactions in both laboratory and astrophysical plasmas, there has been an increasing interest over the last decades in the study of screening effects on the electronic structure of atoms as well as of processes such as photon excitation and ionization, autoionization, electron-atom and ion-atom collisions under the influence of a plasma environment (see the review [3] and references therein). In this respect, some effects in atoms with screened Coulomb interactions have been recently disclosed, such as the red-shift of atomic spectral lines, the important role of low-energy resonances [3,4], and the presence of unexpected Cooper minima in the photoionization spectra of hydrogenlike atoms and ions, issues that have not been addressed in molecules so far. Therefore, a more comprehensive study of new emerging effects arising in molecules under Coulomb screening is pertinent. In the molecular case, only a few studies have been carried out using Yukawa-type screening potentials. For instance, there has been a quest for the stability [5,6] and the presence of Borromean states in the screened molecular ion H_2^+ [7–9], and in screened neutral hydrogen H_2 [10]. The relation between screening and electron correlation in H_2 was also studied for the ground state [11].

Screening effects in many-electron molecules can be incorporated at different levels of sophistication, e.g., from simple effective nuclear charges (without compromising the two-center Coulomb potential and its separability) and Yukawa potentials, to the use of statistical Thomas-Fermi, mean-field Hartree-Fock and variable screening methods [12], inasmuch as the independent molecular orbital approximation is applicable. It is worth noting that the introduction of simple Yukawa interactions in a one-electron molecule brings elements present in the molecular orbital picture of many-electron molecules, namely, the lifting of asymptotic degeneracies [in the separated atoms (SA) and the united atoms (UA) limits], the ubiquitous presence of avoided crossings between adiabatic energy curves and the ensuing dynamical couplings, and new diabatic correlation rules UA $\leftrightarrow$ SA. However, their application is limited since many-body effects that rely on strong electron correlation can never be accounted for with screeninglike model potentials and explicit calculations including electron correlation must be performed.

We present a computational method to study the Yukawa-screened H_2^+ molecule within the Born-Oppenheimer (BO) approximation, which allows us to calculate energies, wave functions, and related properties such as dipole (oscillator strengths) and nonadiabatic couplings. This method allows us

*Present address: Max Born Institute, 12489 Berlin, Germany.
†Corresponding author: jose.sanz@udea.edu.co

to uncover some issues yet unreported, like the drastic variation of energies and wave functions, the lifting of degeneracies resulting in avoided crossings, the presence of molecular shape resonances emerging solely from screening, and the conditions for the appearance of Borromean states within the BO approximation. All these changes in the molecular structure dramatically affect the dynamics of collision processes occurring in Debye plasmas. For instance, photoabsorption and photoionization cross sections of molecules embedded in plasmas have not been reported so far, so that the role of the modified oscillator strengths, molecular shape resonances, and Cooper minima in shaping the cross-section profiles is yet unknown. Also, heavy-particle collisions at low and intermediate velocities in hot dense plasmas can be studied using the molecular model of atomic collisions [13,14], for which the previous computation and analysis of UA-SA energy correlation diagrams and nonadiabatic molecular couplings is a prerequisite.

The paper is organized as follows: In Sec. II we describe our theoretical variational approach based on a partial-wave expansion where the radial function is expressed in terms of B-splines, providing general expressions for the computation of matrix elements for the Hamiltonian, dipole interaction, and nonadiabatic first-derivative radial couplings. In Sec. III we analyze the results related to changes in the electronic structure and properties, namely, molecular energies, wave functions, dipole matrix elements, nonadiabatic couplings, shape resonances, and Borromean states. We finish with some conclusions in Sec. IV. We supplement this work with two Appendixes, that include the implementation of a simple procedure to extract the nodes of our diagonalized unscreened wave functions and a method to avoid the well-known arbitrary sign problem when evaluating molecular couplings. Atomic units (a.u.) are used throughout unless otherwise stated.

II. THEORY

Burrau [15] showed that the two-center Coulomb problem can be separated in the confocal elliptic coordinate system and several authors have reported the solution in terms of the two associated coupled differential equations [16–18], namely, the *inner* equation for the angular η coordinate and the *outer* equation for the radial ξ coordinate. The arrival of computers made available solutions (energies and wave functions) with arbitrary precision (see, for instance, [19–21]) and led to a revival of the problem ([13,22,23] and references therein), including the discovery of an additional dynamical symmetry that yields another constant of motion in the two-center Coulomb problem [24]. With respect to the latter issue, the noncrossing Wigner–von Neumann rule still applies since curves of similar geometrical symmetry exhibiting real crossings have in fact different quantum numbers n_η and n_ξ corresponding to the number of nodes of the eigenstates for the *inner* and *outer* equations, respectively. Screening breaks down this separability and all its related advantages [e.g., an additional constant of motion, factorability of the total wave function making the computation of matrix elements simpler, and avoided crossings and the arbitrary sign problem (discussed in the Appendix)] are not present.

A. Method of solution: Eigenvalue problem

The electronic wave functions $\psi(\mathbf{r},R)$ for the one-electron diatomic molecule (OEDM) are eigensolutions of the Schrödinger equation

$$[\hat{H}(\mathbf{r},R)-E]\Psi(\mathbf{r},R)=0, \tag{1}$$

with the Hamiltonian given by

$$\hat{H}(\mathbf{r},R)=-\tfrac{1}{2}\nabla^2_{\mathbf{r}}+\hat{V}(r_1,r_2;R), \tag{2}$$

where $\mathbf{r}$ is the coordinate vector for the electron, r_1 and r_2 are the distances from the electron to nuclei 1 and 2, respectively, and R is the internuclear distance which acts as a parameter within the BO approximation. As mentioned above, the electronic Hamiltonian for the two-center Coulomb problem, i.e., for $\hat{V}(r_1,r_2;R)=-Z_1/r_1-Z_2/r_2+Z_1Z_2/R$, is separable in confocal elliptic coordinates [15,17]. For the screened potential in the Yukawa form

$$\hat{V}(r_1,r_2;R)=-\frac{Z_1e^{-\lambda r_1}}{r_1}-\frac{Z_2e^{-\lambda r_2}}{r_2}+\frac{Z_1Z_2e^{-\lambda R}}{R}, \tag{3}$$

this separation is no longer possible. However, confocal elliptic coordinates are still the natural coordinates appropriate to look for an accurate variational solution of the Schrödinger equation. In the following, the nuclear repulsion in Eq. (3) is omitted. Confocal elliptic coordinates are defined as

$$\xi=\frac{r_1+r_2}{R}\quad\text{and}\quad\eta=\frac{r_1-r_2}{R} \tag{4}$$

with $1\leqslant\xi<\infty$ and $-1\leqslant\eta\leqslant+1$, along with the azimuthal angle $0\leqslant\phi<2\pi$. In the set of these coordinates the interaction potential (3) reads as

$$\begin{aligned}\hat{V}(\xi,\eta)=&-\frac{2}{R(\xi^2-\eta^2)}[Z_1e^{-\frac{\lambda R}{2}(\xi+\eta)}(\xi-\eta)\\&+Z_2e^{-\frac{\lambda R}{2}(\xi-\eta)}(\xi+\eta)].\end{aligned} \tag{5}$$

We adopt a partial-wave expansion for the electronic wave function $\Psi(\mathbf{r},R)$, where the ξ part is expanded in a basis set in the form

$$\begin{aligned}\Psi^m(\xi,\eta,\phi;R)&=\sum_{\ell=|m|}^{\ell_{max}}\Phi_\ell(\xi)\Theta^m_\ell(\eta)\frac{e^{im\phi}}{\sqrt{2\pi}};\\ \Phi_\ell(\xi)&=\sum_{i=1}^{N_\xi}c^m_{i\ell}\varphi_i(\xi).\end{aligned} \tag{6}$$

In this work, we adopt the basis $\varphi_i(\xi)=(\xi^2-1)^{|m|/2}B_i(\xi)$, where $B_i(x)$ corresponds to a B-spline polynomial [25,26], and $\Theta^m_\ell(\eta)$ is a normalized associated Legendre polynomial, i.e.,

$$\Theta^m_\ell(\eta)=(-1)^m\left[\frac{2\ell+1}{2}\frac{(\ell-m)!}{(\ell+m)!}\right]^{1/2}P^m_\ell(\eta). \tag{7}$$

The expansion coefficients $c^m_{i\ell}$ include the required normalization that allows for $\langle\Psi^m|\Psi^m\rangle=1$. From now on, the label m will be dropped.

If we replace the ansatz (6) [with the expansion in the basis $\varphi_i(\xi)$] in (1) we arrive to a secular equation with Hamiltonian

H and overlap **S** matrices. The Hamiltonian and the overlap matrix elements have the form

$$H_{i\ell,j\ell'} = \frac{R}{4}\{\big[K_{ij} + m^2 C_{ij} + \ell(\ell+1)V_{ij}^{0,0}\big]\delta_{\ell\ell'} - RV_{ij}^{1,-\lambda}\big[Z_1 U_{\ell\ell'}^{0,-\lambda} + Z_2 U_{\ell\ell'}^{0,+\lambda}\big] + RV_{ij}^{0,-\lambda}\big[Z_2\big(a_{\ell m}U_{\ell-1,\ell'}^{0,+\lambda} + a_{\ell+1,m}U_{\ell+1,\ell'}^{0,+\lambda}\big) - Z_1\big(a_{\ell m}U_{\ell-1,\ell'}^{0,-\lambda} + a_{\ell+1,m}U_{\ell+1,\ell'}^{0,-\lambda}\big)\big]\}, \quad (8)$$

and

$$S_{i\ell,j\ell'} = \frac{R^3}{8}\big[V_{ij}^{2,0}\delta_{\ell\ell'} - V_{ij}^{0,0}U_{\ell\ell'}^{2,0}\big], \quad (9)$$

where the explicit integrals to be calculated are

$$K_{ij} = \int_1^\infty d\xi(\xi^2-1)\partial_\xi\varphi_i(\xi)\partial_\xi\varphi_j(\xi), \quad (10)$$

$$C_{ij} = \int_1^\infty d\xi\,\varphi_i(\xi)\varphi_j(\xi)(\xi^2-1)^{-1}, \quad (11)$$

$$V_{ij}^{n,\pm\lambda} = \int_1^\infty d\xi\,\xi^n\varphi_i(\xi)e^{\pm\frac{\lambda R}{2}\xi}\varphi_j(\xi), \quad (12)$$

$$U_{\ell\ell'}^{n,\pm\lambda} = \begin{cases}\int_{-1}^{+1} d\eta\,\eta^n\Theta_\ell^m(\eta)e^{\pm\frac{\lambda R}{2}\eta}\Theta_{\ell'}^m(\eta), & \lambda\neq 0\\ \delta_{\ell\ell'}, & \lambda,n=0\end{cases} \quad (13)$$

and with the angular coefficients

$$a_{\ell m} = [(\ell-m)(\ell+m)/(2\ell-1)(2\ell+1)]^{1/2}. \quad (14)$$

Some angular integrals can be derived in closed form in terms of the latter angular coefficients, for instance, $U_{\ell\ell'}^{2,0} = (a_{\ell m}^2 + a_{\ell+1,m}^2)\delta_{\ell\ell'} + a_{\ell m}a_{\ell-1,m}\,\delta_{\ell,\ell+2} + a_{\ell+1,m}a_{\ell+2,m}\,\delta_{\ell,\ell'-2}$.

Since we choose to use $\varphi_i(\xi) = (\xi^2-1)^{|m|/2}B_i(\xi)$ as the basis function for the radial ξ coordinate, all integrals may be written directly in terms of B-splines and their derivatives and they can be readily computed using Gauss-type quadratures. Indeed, the construction of the Hamiltonian and overlap matrices in terms of B-splines can be reduced to the evaluation of three types of ξ-radial integrals

$$\mathcal{I}_{ij}^{\Delta m,n,\pm\lambda} = \int_1^\infty d\xi(\xi^2-1)^{m+\Delta m}\xi^n e^{\pm\frac{\lambda R}{2}\xi}B_i(\xi)B_j(\xi), \quad (15)$$

$$\mathcal{J}_{ij}^{\Delta m,n} = \int_1^\infty d\xi(\xi^2-1)^{m+\Delta m}\xi^n B_i(\xi)\partial_\xi B_j(\xi), \quad (16)$$

and

$$\mathcal{K}_{ij} = \int_1^\infty d\xi(\xi^2-1)^{m+1}\partial_\xi B_i(\xi)\partial_\xi B_j(\xi), \quad (17)$$

so that the Hamiltonian and overlap matrix elements can be expressed in a suitable computational form as

$$H_{i\ell,j\ell'} = \frac{R}{4}\{\big[m^2\big(\mathcal{I}_{ij}^{-1,2,0} + \mathcal{I}_{ij}^{-1,0,0}\big) + m\big(\mathcal{J}_{ij}^{0,1} + \mathcal{J}_{ji}^{0,1}\big) + \mathcal{K}_{ij} + \ell(\ell+1)\mathcal{I}_{ij}^{0,0,0}\big]\delta_{\ell\ell'} - R\,\mathcal{I}_{ij}^{0,1,-\lambda}\big[Z_1 U_{\ell\ell'}^{0,-\lambda} + Z_2 U_{\ell\ell'}^{0,+\lambda}\big] - R\,\mathcal{I}_{ij}^{0,0,-\lambda}\big[Z_2\big(a_{\ell m}U_{\ell-1,\ell'}^{0,+\lambda} + a_{\ell+1,m}U_{\ell+1,\ell'}^{0,+\lambda}\big) - Z_1\big(a_{\ell m}U_{\ell-1,\ell'}^{0,-\lambda} + a_{\ell+1,m}U_{\ell+1,\ell'}^{0,-\lambda}\big)\big]\}, \quad (18)$$

and

$$S_{i\ell,j\ell'} = \frac{R^3}{8}\big[\mathcal{I}_{ij}^{0,2,0}\delta_{\ell\ell'} - \mathcal{I}_{ij}^{0,0,0}U_{\ell,\ell'}^{2,0}\big]. \quad (19)$$

Once the radial and angular basis set is chosen (the size of the radial ξ box, the number and order of B-splines, and the maximum value for the expansion in angular momenta), the Hamiltonian and overlap matrices are built up to solve the associated generalized eigenvalue problem $(\mathbf{H} - E\mathbf{S})\mathbf{C} = 0$ for each fixed value of $|m| = 0,1,2,\ldots$ $(\sigma,\pi,\delta,\ldots)$. According to the block structure of the Hamiltonian, by using N_ξ B-splines and N_ℓ partial waves (note that $\ell \geqslant |m|$ in the partial-wave expansion), the dimension of the Hamiltonian matrix is $(N_\xi N_\ell)^2$. For most of the calculations reported in this work we have achieved convergence by using $N_\xi = 50$ and $N_\ell = 10$ for both *gerade* (even ℓ's) and *ungerade* symmetries (odd ℓ's). Unlike the unscreened Coulomb case, the analysis of the nodal structure of screened wave functions does not provide unambiguous correlations between atomic quantum numbers in the limits $R = 0$ and $R \to \infty$, although some quasidiabatic correlation rules have been prescribed in the past [12,27]. In this work, we also use the same variational expansions to solve the unscreened Coulomb case ($\lambda = 0$) so that we do not solve the *inner* and *outer* one-dimensional equations with their respective angular and radial nodes. However, in the unscreened case, the number of radial and angular nodes associated to each eigenstate can be easily disclosed at each internuclear distance by a simple inspection of the expansion coefficients in Eq. (6) (see Appendix for details).

B. Radiative dipole matrix elements

Once the eigenvectors of the generalized eigenvalue problem are obtained, one may compute the matrix elements of any operator among them. For instance, the semiclassical treatment for the interaction of the radiation with the molecule involves transition matrix elements in the dipole approximation. In this work, we compute dipole matrix elements among non-screened and screened H_2^+ wave functions, both in the length gauge $\mathbf{r}_{ab} = (x_{ab}, y_{ab}, z_{ab})$ and in the velocity gauge $\mathbf{p}_{ab} = (p_{x,ab}, p_{y,ab}, p_{z,ab})$ between any two eigenstates Ψ_a^m and $\Psi_b^{m'}$.

For the sake of conciseness, we only give the expressions for the z-axis component, that in the case of the length gauge reads as $z_{ab} = \langle\Psi_a|z|\Psi_b\rangle$ with $z = \frac{R}{2}\xi\eta$ (for the origin located at the midpoint of the internuclear distance). From the ansatz (6) one readily obtains

$$z_{ab} = \left(\frac{R}{2}\right)^4\delta_{m_a m_b}\sum_{\ell\ell'}\big[I_{\xi,\ell\ell'}^L J_{\eta,\ell\ell'}^L - J_{\xi,\ell\ell'}^L I_{\eta,\ell\ell'}^L\big],$$

where

$$I_{\xi,\ell\ell'}^L = \sum_{i,j}^{N_\xi} c_{i\ell}^a c_{j\ell'}^b \mathcal{I}_{ij}^{0,3,0} = \mathbf{c}_\ell^{a\dagger}\boldsymbol{I}^{0,3,0}\mathbf{c}_{\ell'}^b, \quad (20)$$

$$J_{\xi,\ell\ell'}^L = \sum_{i,j}^{N_\xi} c_{i\ell}^a c_{j\ell'}^b \mathcal{I}_{i,j}^{0,1,0} = \mathbf{c}_\ell^{a\dagger}\boldsymbol{I}^{0,1,0}\mathbf{c}_{\ell'}^b, \quad (21)$$

$$I^{L}_{\eta,\ell\ell'} = \int_{-1}^{+1} d\eta \Theta^{m_a}_{\ell}(\eta)\Theta^{m_b}_{\ell'}(\eta)\eta^3 \tag{22}$$

$$J^{L}_{\eta,\ell\ell'} = \int_{-1}^{+1} d\eta \Theta^{m_a}_{\ell}(\eta)\Theta^{m_b}_{\ell'}(\eta)\eta. \tag{23}$$

The angular integrals can be easily reduced to the already defined angular coefficients $a_{\ell m}$ and the computational expression can be expressed as

$$z_{ab} = \left(\frac{R}{2}\right)^4 \sum_{\ell} a_{\ell m_a}\{-a_{\ell-2,m_a}a_{\ell-1,m_a}C^{0,1,0}_{\ell,\ell-3,+} + C^{0,3,0}_{\ell,\ell-1,+} - \left(a^2_{\ell-1,m_a} + a^2_{\ell m_a} + a^2_{\ell+1,m_a}\right)C^{0,1,0}_{\ell,\ell-1,+}\}\delta_{m_a m_b}, \tag{24}$$

where the terms $C^{\Delta m,n,\lambda}_{\ell,\ell',\pm}$ are obtained from vector-matrix multiplications between expansion coefficients vectors in (6) and the matrices defined in (15) [as follows from (20) and (21)]:

$$C^{\Delta m,n,-\lambda}_{\ell,\ell',\pm} = \mathbf{c}^{a\dagger}_{\ell}\boldsymbol{I}^{\Delta m,n,-\lambda}\mathbf{c}^{b}_{\ell'} \pm \mathbf{c}^{b\dagger}_{\ell}\boldsymbol{I}^{\Delta m,n,-\lambda}\mathbf{c}^{a}_{\ell'}.$$

Similarly, in the velocity gauge, the z component reads as $p_{z,ab} = -i\langle\Psi_a|\partial/\partial z|\Psi_b\rangle$ and, with the z derivative given by $\frac{\partial}{\partial z} = \frac{2}{R}\frac{1}{\xi^2-\eta^2}[(\xi^2-1)\eta\frac{\partial}{\partial\xi} + (1-\eta^2)\xi\frac{\partial}{\partial\eta}]$ in confocal elliptic coordinates, these matrix elements can be computed using the algorithm

$$p_{z,ab} = -i\left(\frac{R}{2}\right)^2\delta_{m_a m_b} \times \sum_{\ell} a_{\ell m}\left[D_{\ell,\ell-1} - (\ell-m-1)C^{0,1,0}_{\ell,\ell-1,-}\right], \tag{25}$$

where $D_{\ell,\ell'}$ comes from the vector-matrix multiplication

$$D_{\ell,\ell'} = \mathbf{c}^{a\dagger}_{\ell}\boldsymbol{J}^{1,0}\mathbf{c}^{b}_{\ell'} - \mathbf{c}^{b\dagger}_{\ell}\boldsymbol{J}^{1,0}\mathbf{c}^{a}_{\ell'},$$

where $\boldsymbol{J}$ is the matrix defined in Eq. (16).

C. Nonadiabatic radial couplings

Nonadiabatic radial couplings involve first and second derivatives with respect to the internuclear distance, i.e., $\hat{A} = \frac{d}{dR}|_{\mathbf{r}}$ and $\hat{B} = \frac{d^2}{dR^2}|_{\mathbf{r}}$. In terms of a complete basis of eigenstates, the matrix for the second derivatives can be obtained from the first derivative matrix elements $\mathbf{B} = \mathbf{A}^2 + d\mathbf{A}/dR$ [13,28]. To obtain such a complete basis of eigenstates is computationally within reach for $H_2{}^+$. Thus, we evaluate here only the first derivative couplings between screened $H_2{}^+$ eigenfunctions. The anti-Hermitian operator $\hat{A}$ can be split into in three terms $\hat{A} = \partial/\partial R|_{\xi,\eta} + \partial\xi/\partial R|_{\mathbf{r}}\,\partial/\partial\xi|_{R,\eta} + \partial\eta/\partial R|_{\mathbf{r}}\,\partial/\partial\eta|_{R,\xi}$. Although we use variational wave functions, their energy usually has 9 to 10 significant figures (as compared, for example, to the exact ones in the unscreened case). After such consideration, the first term in $\hat{A}$ can be obtained from the nondiagonal Hellman-Feynman theorem, i.e., $\langle\Psi_a|\partial/\partial R|_{\xi,\eta}|\Psi_b\rangle = -\langle\Psi_a|\partial\hat{H}/\partial R|\Psi_b\rangle/(E_a - E_b)$, which in the screened case reduces to evaluate the matrix elements of the operator

$$\frac{\partial\hat{H}}{\partial R} = -\frac{2}{R}\hat{H} + \frac{1}{R}\hat{V} + \frac{\lambda}{R}e^{-\frac{\lambda R}{2}\xi}(Z_1 e^{-\frac{\lambda R}{2}\eta} + Z_2 e^{+\frac{\lambda R}{2}\eta}). \tag{26}$$

In terms of our ansatz (6) for the eigenvectors, the computational algorithm for the matrix elements of the operator (26) reads as

$$\langle\Psi_a|\partial\hat{H}/\partial R|\Psi_b\rangle = \delta_{m_a m_b}\left\{\frac{1}{R}\mathbf{c}^{\dagger a}\mathbf{V}\mathbf{c}^{b} + \lambda\frac{R^2}{8}\sum_{\ell,\ell'}\left[\left(Z_1 U^{0,-\lambda}_{\ell\ell'} + Z_2 U^{0,+\lambda}_{\ell,\ell'}\right) \times \mathbf{c}^{\dagger a}_{\ell}\boldsymbol{I}^{0,2,-\lambda}\mathbf{c}^{b}_{\ell'} - \left(Z_1 U^{2,-\lambda}_{\ell\ell'} + Z_2 U^{2,+\lambda}_{\ell,\ell'}\right)\mathbf{c}^{\dagger a}_{\ell}\boldsymbol{I}^{0,0,-\lambda}\mathbf{c}^{b}_{\ell'}\right]\right\}. \tag{27}$$

For the second term in the radial coupling operator, $\partial\xi/\partial R|_{\mathbf{r}}\partial/\partial\xi|_{R,\eta}$, it is required to compute

$$\langle\Psi_a|\frac{\xi}{R}\frac{\xi^2-1}{\xi^2-\eta^2}\frac{\partial}{\partial\xi}|\Psi_b\rangle = \frac{R^2}{16}\delta_{m_a m_b}\sum_{\ell}\mathbf{c}^{\dagger a}_{\ell}[\boldsymbol{J}^{1,1} - \boldsymbol{J}^{\dagger 1,1} - 3\boldsymbol{I}^{0,2,0} + \boldsymbol{I}^{0,0,0}]\mathbf{c}^{b}_{\ell}, \tag{28}$$

whereas for the third term $\partial\eta/\partial R|_{\mathbf{r}}\partial/\partial\eta|_{R,\xi}$, the computation requires the matrix element

$$\langle\Psi_a|\frac{\eta}{R}\frac{1-\eta^2}{\xi^2-\eta^2}\frac{\partial}{\partial\eta}|\Psi_b\rangle = \frac{R^2}{8}\delta_{m_a m_b}\left\{\sum_{\ell}(\ell+1)a_{\ell m}a_{\ell-1,m}\mathbf{c}^{b\dagger}_{\ell-2}\boldsymbol{I}^{0,0,0}\mathbf{c}^{a}_{\ell} + \sum_{\ell}\left[(\ell+1)a^2_{\ell m} - \ell a^2_{\ell+1,m}\right]\mathbf{c}^{a\dagger}_{\ell}\boldsymbol{I}^{0,0,0}\mathbf{c}^{b}_{\ell} - \sum_{\ell}(\ell-2)a_{\ell m}a_{\ell-1,m}\mathbf{c}^{a\dagger}_{\ell}\boldsymbol{I}^{0,0,0}\mathbf{c}^{b}_{\ell-2}\right\}. \tag{29}$$

We have checked numerically that the collection of the three terms in the operator $\hat{A}$ yields an antisymmetric matrix $\mathbf{A}$. Our radial couplings for the unscreened case ($\lambda = 0$) also compare very well with those available in the literature [29–31]. It is well known that nonadiabatic couplings depend on the origin of the coordinate frame [13,32]. Our radial couplings in this work are calculated for the origin located at the geometrical center of the two nuclei (for $H_2{}^+$ it coincides with the nuclear center of mass). Corrections to the radial couplings due to a shift $\pm\delta R$ (with $\delta \in [-\frac{1}{2}, +\frac{1}{2}]$) from the origin at the midpoint along the internuclear distance $Z_1 O Z_2$ in the z axis ($O \to O \pm \delta R$) involve an extra term $\mp i\frac{\delta R}{R}\hat{p}_z$, which involves the z component of the dipole operator in the velocity gauge, whose evaluation has been treated in the previous Sec. II B.

III. RESULTS

A. Potential energy curves of screened $H_2{}^+$

In Fig. 1 we plot the variation of the total electronic energies for the lowest states in $H_2{}^+$ calculated at the internuclear distance $R = 2$ a.u. against $\lambda \in [0, 1.6]$ a.u. Electronic states in $H_2{}^+$ tend to increase their electronic energy (without nuclear interaction) monotonically as the screening increases, until they cross the limit $E = 0$ a.u.. When the nuclear interaction is added at a given internuclear distance R, the corresponding energy curves for highly excited states show a maximum with

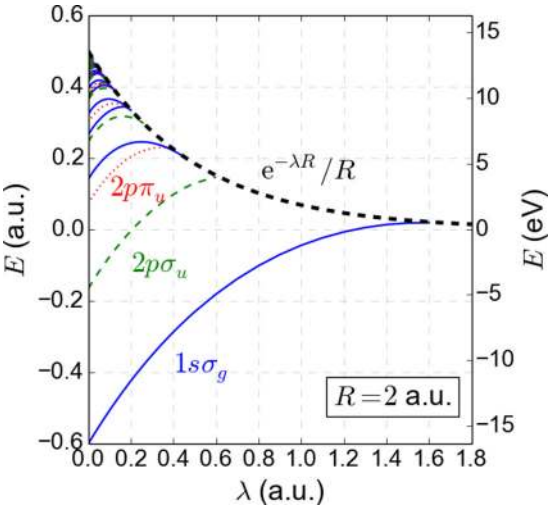

FIG. 1. Electronic energies (plus nuclear repulsion $e^{-\lambda R}/R$) for the 15 lowest electronic states of symmetry σ_g (solid blue lines), σ_u (green dashed lines), and π_u (red dotted lines) of H_2^+ as a function of the screening parameter λ at the (unscreened) equilibrium internuclear distance $R = 2$ a.u. Only the ($\lambda = 0$) labels for the three lowest states $1s\sigma_g$, $2p\sigma_u$, and $2p\pi_u$ are included. The ionization threshold for screened H_2^+ ($e^{-\lambda R}/R$ for $R = 2$ a.u.) is also included (black thick-dashed line). The crossings of the energies of the electronic states with the ionization threshold curve indicate the value of the screening parameter λ at which the states become unbound.

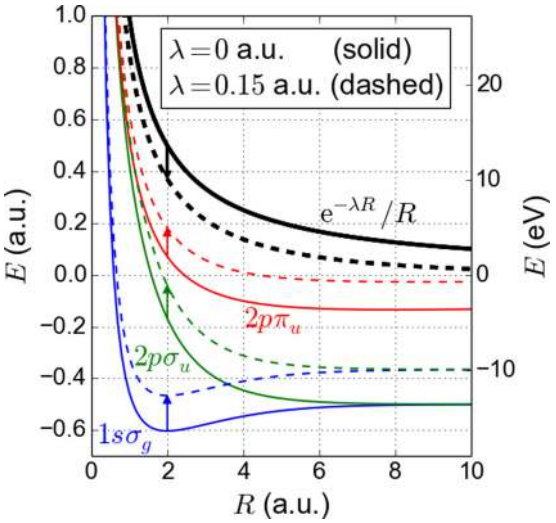

FIG. 2. Electronic energies (plus nuclear repulsion $e^{-\lambda R}/R$) for the three lowest electronic states of H_2^+ as a function of the internuclear distance R, for the unscreened case ($\lambda = 0$, with solid lines) and for a weakly screened case ($\lambda = 0.15$ a.u., with dashed lines). Labels for the unscreened three lowest states $1s\sigma_g$ (blue solid line), $2p\sigma_u$ (green solid line), and $2p\pi_u$ (red solid line) are indicated as well as the ionization threshold ($e^{-\lambda R}/R$) for $\lambda = 0$ (black thick-solid line) and $\lambda = 0.15$ a.u. (black thick-dashed line). Vertical arrows indicate the energy shift of the four levels at the internuclear distance $R = 2$ a.u. due to the screening effect.

respect to λ before crossing the upper continuum threshold, i.e., they do not monotonically increase (see Fig. 1) although, in other words, the electronic binding energy always decreases monotonically with λ.

The energy variation with λ slightly depends on the internuclear distance R for a relatively weak screening (see Fig. 2). For such weak cases, the screened interaction potential in Eq. (3) can be expanded in series, and to first order in λ can simply be written as $\hat{V}(\lambda = 0) + (Z_1 + Z_2 - Z_1 Z_2)\lambda$, i.e., the dominant effect is a linear increase of the molecular energies with λ. This linear behavior of the electronic energies, $E_n + \lambda$, in H_2^+ ($Z_1 = Z_2 = 1$) for weak screening (up to $\lambda = 0.2$ a.u.) is clearly observed in Fig. 1 for deeply bound states such as $1s\sigma_g$ and $2p\sigma_u$. In this range, $\lambda \in [0,0.2]$ a.u., the energies of $2p\pi_u$ and higher-lying excited states are much more affected by the following term $O(\lambda^2)$ in the series expansion $\frac{1}{2}(-Z_1 r_1 - Z_2 r_2 + Z_1 Z_2 R)\lambda^2$, which for H_2^+ gives a negative contribution since $\langle r_1 \rangle = \langle r_2 \rangle > R/2$. The average value of $\langle r_i \rangle_{i=1,2}$ also increases with the excitation, so that the energy profile against λ for highly excited states becomes an inverted parabola. Notice that Fig. 1 shows some apparent energy crossings close to the continuum limit, for instance, the lowest π_u ($2p\pi_u$) and the second lowest σ_g ($2s\sigma_g$) states. In fact, they cross the upper threshold at different λ's, 0.38 and 0.42 a.u., respectively, so that they cross each other before meeting the continuum threshold. The maximum of the inverted parabolas is approximately given (to second order) by $\lambda = \frac{1}{2(\langle r_1 \rangle - 1)}$ so that it is connected with the inverse of the spatial extension of the state. As excitation increases (more diffuse states), the maximum of the parabola shifts to smaller λ. The concavity also depends upon the wave-function structure through $\langle r_1 \rangle$, so that, in principle, all parabolas could have crossings at some point. The crossing point of two different energy curves (which incidentally may coincide with the ionization threshold curve) depends approximately on the squared root of the ratio between their energy difference and their $\langle r_1 \rangle$ difference at $\lambda = 0$. Ultimately, it may be that a triple crossing at threshold happens just by chance.

The unscreened H_2^+ molecular ion has an infinite number of electronic bound states due to the Coulomb potential tail. However, screening not only makes this number finite, but it also decreases dramatically with increasing λ. At each internuclear distance, there is a critical value of λ for each molecular state at which its energy crosses the ionization limit $e^{-\lambda R}/R$ and it becomes unbound. For instance, as shown in Fig. 1 at $R = 2$ a.u., the $2p\pi_u$ state no longer exists beyond $\lambda \sim 0.4$ a.u., the $2p\sigma_u$ state disappears for $\lambda \sim 0.6$ a.u., and the ground state requires a screening strength $\lambda \sim 1.7$ a.u. to become unbound. Highly lying states require even smaller values of the screening strength to become unbound. It is worth noting that the validity of the Debye-Hückel model of screening is limited and results for Debye lengths $D = 1/\lambda$ shorter than the atomic size must be taken with caution as they are mostly qualitative.

As an additional illustration, we show in Fig. 2 the potential energy curves for the three lowest states $1s\sigma_g$, $2p\sigma_u$, and $2p\pi_u$ for the unscreened case ($\lambda = 0$) and a particular softly screened case ($\lambda = 0.15$ a.u.). Note that, for the sake of simplicity, we keep in this work the same (although inappropriate) nomenclature for the screened states. The molecular energies for the screened case are shifted up approximately by the constant factor $\lambda = 0.15$ a.u. Similarly,

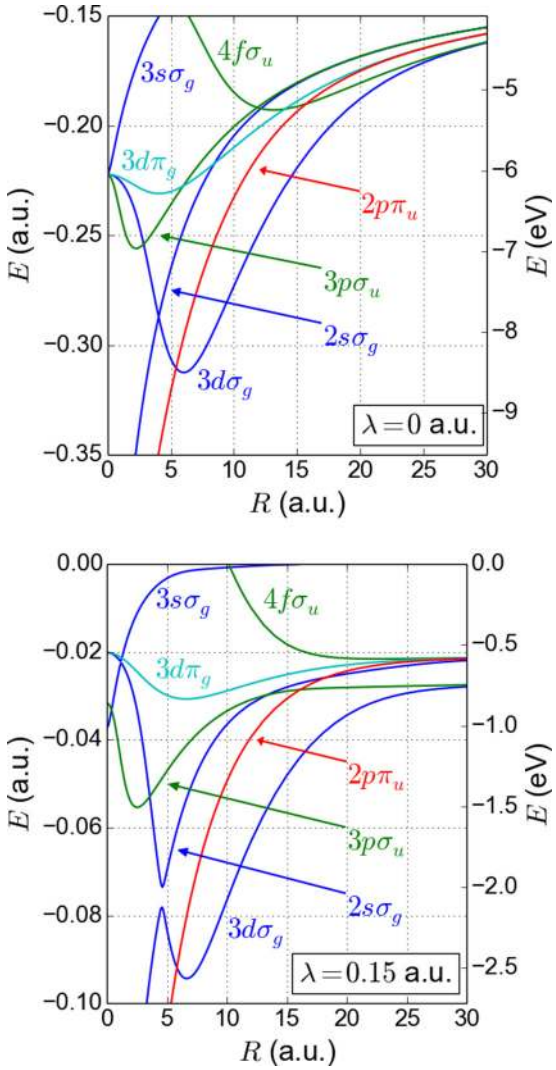

FIG. 3. Detail of the electronic energies (without the nuclear repulsion term $e^{-\lambda R}/R$) of unscreened ($\lambda = 0$, top panel) and screened ($\lambda = 0.15$ a.u., bottom panel) H_2^+ in the region of states dissociating into $H(n = 2) + H^+$. Notation for unscreened OEDM states ($n\ell|m|_{g,u}$) is used in both cases.

the molecular ionization threshold given by $e^{-\lambda R}/R$ (which eventually leads to a slower Yukawa explosion than the usual Coulomb one) shifts down by a similar amount. As a consequence, the molecular continuum lowers.

In order to appreciate more substantial changes in the electronic energies, one can explore higher excited states for which the energy behavior against λ strongly departs from linearity. For instance, we look at the manifold of molecular states of H_2^+ dissociating into $H(n = 2) + H^+$, which for the unscreened case corresponds to the set $\{2p\pi_u, 2s\sigma_g, 3p\sigma_u, 3d\sigma_g, 3d\pi_g$, and $4f\sigma_u\}$. A detail of the electronic curves of these states is given in Fig. 3 for the unscreened case and for a relatively weak screening of $\lambda = 0.15$ a.u. It is worth noticing that (i) as the energies are shifted up with screening, the state $4f\sigma_u$ correlating to $He^+(n = 4)$ in the united atom (UA) limit in the unscreened case is no longer bound below $R = 10$ a.u. (this effect has been previously termed electron promotion into the continuum as a mechanism for vacancy production within the quasimolecular picture of atomic collisions [12]); (ii) the degeneracy of the levels $He^+(n = 3)$ in the UA limit ($E = 2/9$ a.u.) is lifted to yield separate $He^+(3s)$, $He^+(3p)$, and $He^+(3d)$ energy levels with $E_{3s} < E_{3p} < E_{3d}$, energies that match those obtained with a separate one-electron atomic code; (iii) degeneracy is also removed in the separated atom (SA) limit so that one can distinguish between states that correlate to $H(2s)$ and $H(2p)$, and (iv) real crossings in unscreened H_2^+ transform into avoided crossings due to the breaking of the dynamical symmetry associated to the separation constant [24]. Three anticrossings can be seen in Fig. 3 for $\lambda = 0.15$ a.u.: a sharp one between $2s\sigma_g$ and $3d\sigma_g$ (blue lines) located at $R \sim 4.5$ a.u., another one between $2s\sigma_g$ and $3s\sigma_g$ (blue lines) located at $R \sim 1$ a.u. [due to the energy splitting of $He^+(n = 3)$ at $R = 0$], and a diffuse one between $3p\sigma_u$ and $4f\sigma_u$ (green lines) at $R > 12$ a.u. The diffuse character of the latter is partly due to the different SA correlation limits of the two involved states and, at variance with the Coulomb case, the similarity of the UA energies for $He^+(n = 3)$ and the SA energies for $H(n = 2)$ due to screening. In addition, the subshell splitting $2s - 2p$ at $R \to \infty$ is larger than the Stark splitting at intermediate distances. The presence and shape of these avoided crossings may have its effect in the calculation of the coupled vibronic structure or in collisional phenomena due to the presence of nonadiabatic couplings among states, which are particularly large in the region of anticrossings (see below).

B. Borromean states in H_2^+

The system H_2^+ has already been the target in the quest for Borromean states [7–9] as a prototypical molecular three-body system. H_2^+ is said to be in a Borromean state if under given circumstances the three-body system is bound while the corresponding two-body subsystems ($H^+ - e^-$ and $H^+ - H^+$) are unbound. Screened interactions among the three particles may produce such particular situation. The calculations mentioned previously [7–9] made use of a direct three-body approach (beyond the BO approximation) using explicitly correlated coordinates, to obtain accurate solutions for the lowest molecular levels. The lowest rotation-vibration state for the $1s\sigma_g$ state corresponds to their computed *atomiclike* state $^1S^e(v = 0, J = 0)$. They showed that this ground state is no longer bound beyond $\lambda = 1.37$ a.u., whereas the hydrogen atom has no bound states beyond $\lambda = 1.19$ a.u. This fact indicates the presence of a window $1.19 < \lambda < 1.37$ a.u. in which Borromean states of H_2^+ exist. Without being exhaustive in our search, we have explored this subject within the BO approximation, which means to find the critical screening value for which the molecular energy curve $1s\sigma_g$ does not support vibrational states anymore.

Recently, Wu *et al.* [33] have reported the calculation of vibrational states of screened H_2^+, between $\lambda = 0$ and 0.71 a.u. For that purpose, they adapted a molecular multireference configuration interaction (MRD-CI) code based on Gaussian basis sets. In order to carry out the integrals for the screened Coulomb interaction, the Yukawa potential was also expanded in terms of a few Gaussian functions. They showed that, since the internuclear equilibrium distance increases, the

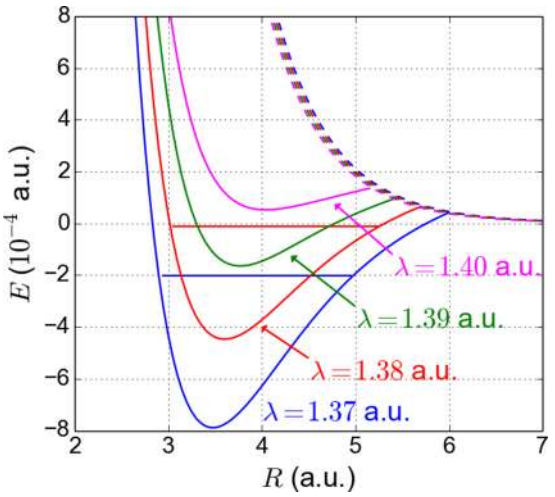

FIG. 4. Potential energy curves (including the nuclear repulsion) of the ground state $1s\sigma_g$ (solid lines) of screened H_2^+ for three large screening parameters $\lambda = 1.37$ a.u. (blue), $\lambda = 1.38$ a.u. (red), $\lambda = 1.39$ a.u. (green), and $\lambda = 1.40$ a.u. (pink). The curves of the ground state are drawn until they cross their respective upper ionization potential curve $e^{-\lambda R}/R$ (dashed curves with the same scheme of colors for the λ's, and note that the continuum threshold shifts down with increasing λ). Whereas the electronic ground state supports a single vibrational state for $\lambda = 1.37$ and 1.38 a.u., this is not the case for $\lambda = 1.39$ and 1.40 a.u., whose potential curves show a minimum below and above the dissociative threshold at $E = 0$ a.u., respectively.

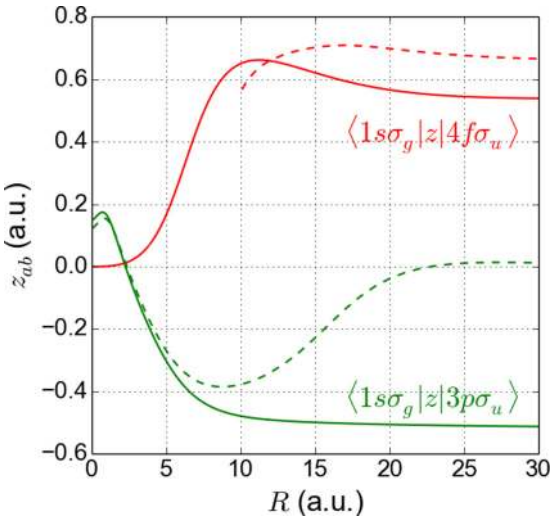

FIG. 5. Dipole matrix elements (length gauge) between the ground state $1s\sigma_g$ and the $3p\sigma_u$ and $4f\sigma_u$ states (the states with energies included in Fig. 3 and wave functions in Fig. 6) as a function of the internuclear distance for the unscreened case ($\lambda = 0$, with solid lines) and a particular screened case ($\lambda = 0.15$ a.u. with dashed lines). The dipole matrix element $\langle 1s\sigma_g|z|4f\sigma_u\rangle$ starts from $R = 10$ a.u. in the screened case because $4f\sigma_u$ is unbound below this internuclear distance (see Fig. 3). Whereas in the unscreened case both σ_u states are coupled with the ground state in the SA limit, the dipole coupling $\langle 1s\sigma_g|z|3p\sigma_u\rangle$ in the screened case vanishes asymptotically (see text).

potential curve widens and simultaneously the dissociation energy decreases when the screening strength increases, the number of vibrational states in the range $\lambda \in [0,0.71]$ remains practically constant around 20. Due to their limitation in the representation of the molecular Yukawa potential with Gaussians, they cannot analyze this issue beyond $\lambda = 0.71$ a.u. Our present BO method of solution is superior to that of [33] in the representation of the screened interactions and we are not limited to small-λ values. We have checked that their quasiconservation conjecture does not hold for $\lambda > 0.71$ a.u. and the number of vibrational states supported by the curve $1s\sigma_g$ reduces, up to a critical value $\lambda = 1.38$ a.u. for which only one vibrational state survives with negative energy below the dissociative ionization limit $E = 0$ a.u. (see Fig. 4). In fact, we have used a code based on both large B-splines expansions and radial boxes to solve the nuclear equation and we find only one vibrational state with energy $E_{v=0} = -2.02 \times 10^{-4}$ a.u. for $\lambda = 1.37$ a.u., also a single vibrational state with energy $E_{v=0} = -1.11 \times 10^{-5}$ a.u. for $\lambda = 1.38$ a.u. and, although the energy curve for $\lambda = 1.39$ a.u. displays a minimum below $E = 0$ a.u., we were unable to find any supported bound state. Our value $\lambda = 1.38$ a.u. is similar to the upper limit for the existence of Borromean states predicted by other authors using methods that go beyond the BO approximation [7–9]. Although, at first sight, it may seem unreasonable to use the BO approximation to characterize a system with such small electronic energies, the agreement with previous NBO results is remarkable.

C. Radiative dipolar couplings

Dipole couplings (following the computational recipe given in Sec. II B) can be computed between any two pair of screened OEDM states, allowed by the same selection rules as for the unscreened case, namely, the $g \leftrightarrow u$ parity rule, and the Δm rule for parallel (0) and perpendicular transitions (± 1) concerning the orientation of the polarization vector with respect to the internuclear direction. As a particular illustration of the calculation of dipole couplings, we plot in Fig. 5 the dipole matrix elements between the ground $1s\sigma_g$ state and the $3p\sigma_u$ and $4f\sigma_u$ states. Note that the latter two states correlate to $H(n = 2)$ in the SA limit. In the unscreened case, it is well known that the state $3p\sigma_u$ correlates in the UA limit to the $He^+(3p)$ state and to the Stark combination (due to the long-range Coulomb interaction)

$$\psi_{3p\sigma_u} = \frac{1}{\sqrt{2}}\left[\frac{1}{\sqrt{2}}(\phi_{2s} + \phi_{2p_z})(\mathbf{r}_1) - \frac{1}{\sqrt{2}}(\phi_{2s} - \phi_{2p_z})(\mathbf{r}_2)\right]$$

in the SA limit. Similarly, the state $4f\sigma_u$ tends to $He^+(4f)$ in the UA limit and to the Stark combination

$$\psi_{4f\sigma_u} = \frac{1}{\sqrt{2}}\left[\frac{1}{\sqrt{2}}(\phi_{2s} + \phi_{2p_z})(\mathbf{r}_2) - \frac{1}{\sqrt{2}}(\phi_{2s} - \phi_{2p_z})(\mathbf{r}_1)\right]$$

in the SA limit. This UA-SA correlation for the OEDM unscreened wave functions is plotted in the upper panels of Fig. 6 for three selected internuclear distances $R = 2$, 12, and 25 a.u. Note that $\mathbf{r}_1$ ($\mathbf{r}_2$) corresponds to electronic coordinates associated to the lower (upper) nucleus in this figure. Asymptotic UA and SA values for the dipole matrix elements with the operator $\hat{z}$ in the length gauge can be derived

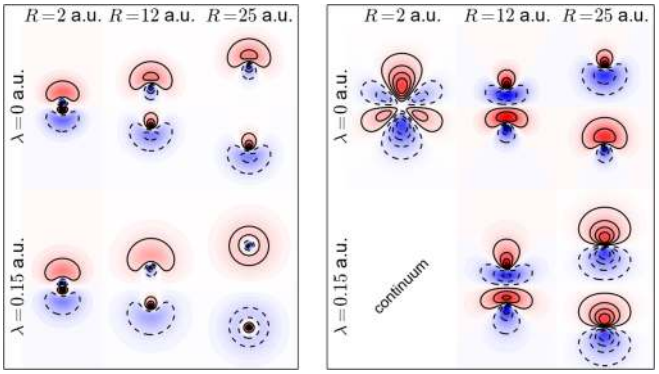

FIG. 6. Evolution of the wave functions corresponding to states $3p\sigma_u$ (left) and $4f\sigma_u$ (right) of H_2^+ for three representative internuclear distances ($R = 2$, 12, and 25 a.u.) along the UA-SA molecular correlation diagram, both in the unscreened ($\lambda = 0$) and a particular screened case ($\lambda = 0.15$ a.u.). The wave functions are drawn as contour plots in the XZ plane where the internuclear distance R lies along the Z axis. Red shadows indicate areas in which the wave function is positive valued and blue shaded areas are those regions with negative values. In the unscreened case ($\lambda = 0$), both states tend to a superposition of Stark states whereas in the screened case the $3p\sigma_u$ and the $4f\sigma_u$ clearly tend upon dissociation to spherical $2s$ and $2p_z$ states, respectively. As quoted in Fig. 3, the $4f\sigma_u$ state is not bound at the internuclear distance $R = 2$ a.u.

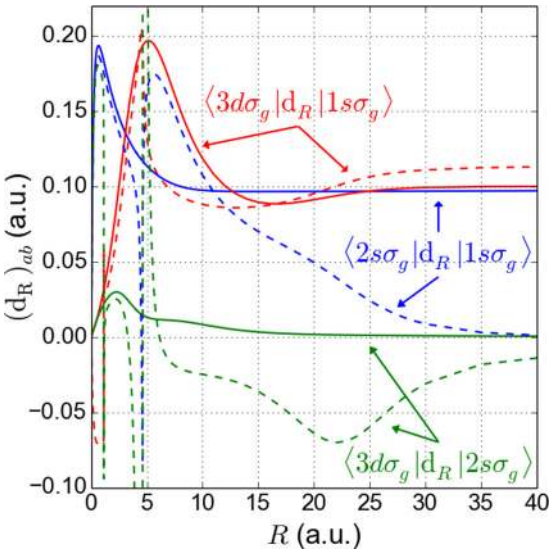

FIG. 7. Radial coupling matrix elements between the three lowest σ_g states: $1s\sigma_g$, $2s\sigma_g$, and $3d\sigma_g\langle 2s\sigma_g|\partial/\partial R|1s\sigma_g\rangle$ (in blue), $\langle 3d\sigma_g|\partial/\partial R|1s\sigma_g\rangle$ (in red), and $\langle 3d\sigma_g|\partial/\partial R|2s\sigma_g\rangle$ (in green) for the unscreened case ($\lambda = 0$ a.u., with solid lines) and the screened case ($\lambda = 0.15$ a.u., with dashed lines).

analytically from the above expressions, so that, in the screened case $\langle\psi_{1s\sigma_g}|z|\psi_{3p\sigma_u}\rangle$ goes to $\langle\phi_{1s}|z|\phi_{3p_z}\rangle_{He^+} = 0.1492$ a.u. in the UA limit and $-\frac{1}{\sqrt{2}}\langle\phi_{1s}|z|\phi_{2p_z}\rangle_H = -0.5267$ a.u. in the SA limit. Similarly, $\langle\psi_{1s\sigma_g}|z|\psi_{4f\sigma_u}\rangle$ starts from $\langle\phi_{1s}|z|\phi_{4f_z}\rangle_{He^+} = 0$ at $R = 0$ and goes to $\frac{1}{\sqrt{2}}\langle\phi_{1s}|z|\phi_{2p_z}\rangle_H = 0.5267$ a.u. at $R \to \infty$. In the screened case, explicit computations for the dipole couplings are required at any distance. For instance, using a moderate screening value $\lambda = 0.15$ a.u., the formation of Stark states is still robust at intermediate distances (see lower panels in Fig. 6 for $R = 12$ a.u.) but eventually these screened OEDM states tend to spherical states asymptotically {the $3p\sigma_u$ tends to $\frac{1}{\sqrt{2}}[\phi^\lambda_{2s}(\mathbf{r}_1) - \phi^\lambda_{2s}(\mathbf{r}_2)]$ and the $4f\sigma_u$ tends to $\frac{1}{\sqrt{2}}[\phi^\lambda_{2p_z}(\mathbf{r}_1) + \phi^\lambda_{2p_z}(\mathbf{r}_2)]$} as clearly appreciated in Fig. 6. In this screened case, in the SA limit, $\langle\psi^\lambda_{1s\sigma_g}|z|\psi^\lambda_{3p\sigma_u}\rangle$ clearly vanishes and $\langle\psi^\lambda_{1s\sigma_g}|z|\psi^\lambda_{4f\sigma_u}\rangle$ tends to $\langle\phi^\lambda_{1s}|z|\phi^\lambda_{2p_z}\rangle$, this time evaluated numerically with screened atomic orbitals (in the unscreened case this matrix element takes the value $\langle\phi_{1s}|z|\phi_{2p_z}\rangle = \frac{2^7\sqrt{2}}{3^5} = 0.7449$ a.u.). Similar detailed analysis can be carried out with all electronic states.

In conclusion, whereas unscreened OEDMs are always $g - u$ coupled at all distances due to the Stark mixing, screening breaks this Stark mixing and therefore provokes the damping of the couplings between those OEDMs which now tend to dipole-uncoupled spherical states. The trend for couplings and the breaking of energy degeneracies is analogous to that observed when moving from one-electron to many-electron molecules. In this direction, our screened one-electron model may serve as a simple prototype to analyze some properties expected to appear in many-electron molecules but at a lower computational cost. Indeed, in the context of inner-shell vacancy production in the quasimolecular model of atomic collisions involving many-electron atoms, screened molecular orbitals were generated by extending the Yukawa potentials in (3) to single-electron potentials $v(r_i) = -\frac{Z_i}{r_i}\chi(r_i;\alpha)$, where *universal* R-variable screening functions $\chi(r_i;\alpha)$ were adjusted through the effective parameter α to reproduce Thomas-Fermi potentials in the UA and SA limits (see, for instance, [12] and references therein).

D. Nonadiabatic radial couplings

The asymptotic values for the radial couplings can be readily estimated from the LCAO molecular wave functions. For instance, in the unscreened case, the radial coupling value at $R \to \infty$ between the $1s\sigma_g$ and the $3d\sigma_g$ states, i.e., $\langle\psi_{3d\sigma_g}|\frac{\partial}{\partial R}|\psi_{1s\sigma_g}\rangle$, can be obtained by using (i) $\psi_{1s\sigma_g} = \frac{1}{\sqrt{2}}[\phi_{1s}(\mathbf{r}_1) + \phi_{1s}(\mathbf{r}_2)]$ and the Stark combination $\psi_{3d\sigma_g} = \frac{1}{\sqrt{2}}\ [\frac{1}{\sqrt{2}}(\phi_{2s} - \phi_{2p_z})(\mathbf{r}_1) + \frac{1}{\sqrt{2}}(\phi_{2s} + \phi_{2p_z})(\mathbf{r}_2)]$, (ii) the chain rule $\frac{\partial}{\partial R} = \frac{\partial z_{1,2}}{\partial R}\frac{\partial}{\partial z_{1,2}} = \pm\frac{1}{2}\frac{\partial}{\partial z_{1,2}}$, and (iii) the gauge relation $\langle\phi_{2p_z}|p_z|\phi_{1s}\rangle = i(E_{2p} - E_{1s})\langle\phi_{2p_z}|z|\phi_{1s}\rangle$. By using $\langle\phi_{2p_z}|z|\phi_{1s}\rangle = \frac{2^7\sqrt{2}}{3^5}$, this radial coupling simply yields $\frac{2^3}{3^4} \sim 0.098765$ in agreement with our result at large R in Fig. 7. The radial coupling $\langle\psi_{2s\sigma_g}|\frac{\partial}{\partial R}|\psi_{1s\sigma_g}\rangle$ must have the same asymptotic absolute value since $\psi_{2s\sigma_g} = \frac{1}{\sqrt{2}}\ [\frac{1}{\sqrt{2}}(\phi_{2s} + \phi_{2p_z})(\mathbf{r}_1) + \frac{1}{\sqrt{2}}(\phi_{2s} - \phi_{2p_z})(\mathbf{r}_2)]$. Similarly, it can be shown by using the LCAO wave functions that $\langle\psi_{3d\sigma_g}|\frac{\partial}{\partial R}|\psi_{2s\sigma_g}\rangle$ vanishes at $R \to \infty$.

In contrast, in the screened case, the UA-SA correlation rules are different [12,14]. The screening produces a similar effect as in the many-electron case, where the degeneracy at the SA and UA limits is removed and some real crossings that appear in the unscreened case appear now as avoided crossings. The representative case is the pair of screened OEDMs $2s\sigma_g$ and $3d\sigma_g$, whose energies show an avoided crossing just below

$R = 5$ a.u. for the screening parameter $\lambda = 0.15$ a.u. (see Fig. 3). Following the Barat-Lichten rules [27] or a smooth topological correlation rule [14], the $2s\sigma_g$ state exchanges its Stark mixing form with that of the $3d\sigma_g$ state. This Stark mixing is effective only at intermediate internuclear distances, but eventually (due to the loss of infinite-range Coulomb potential) the Stark states tend to hydrogenic orbitals (as illustrated in Fig. 6). In the screened case, the $2s\sigma_g$ molecular orbital tends to the LCAO combination $\frac{1}{\sqrt{2}}[\phi_{2s}(\mathbf{r}_1) + \phi_{2s}(\mathbf{r}_2)]$, whereas the $3d\sigma_g$ orbital tends to the LCAO combination $\frac{1}{\sqrt{2}}[\phi_{2p_z}(\mathbf{r}_1) - \phi_{2p_z}(\mathbf{r}_2)]$. This leads to an asymptotically vanishing coupling $\langle 2s\sigma_g|\frac{\partial}{\partial R}|1s\sigma_g\rangle$ in the screened case. However, the radial coupling $\langle 3d\sigma_g|\frac{\partial}{\partial R}|1s\sigma_g\rangle$ goes to a constant value that depends on the screening strength λ and asymptotically nonvanishing couplings must be calculated computationally. Note that the apparent discontinuities in the radial couplings plotted in Fig. 7 are due to the presence of avoided crossings between the screened $2s\sigma_g$ and $3d\sigma_g$ states around $R \sim 4.5$ a.u. and between $2s\sigma_g$ and $3s\sigma_g$ states around $R \sim 1$ a.u. (see Fig. 3).

E. Shape resonances in screened H_2^+

It is known that, unlike the Coulomb potential, a Yukawa potential for a single electron atom has shape resonances in the continuum structure [4]. This means that screened H_2^+ must have shape resonances in both the UA ($R = 0$) and SA ($R \to \infty$) limits, so that it is pertinent to investigate if such states can survive beyond those atomic limits. In fact, in the atomic context, these resonances lie very close to the ionization threshold and its origin comes from the presence of a relatively small effective potential barrier.

To explore the presence of these shape resonances in screened H_2^+, we use the stabilization method [34]. This method aims at evaluating the density of states in selected regions of the electronic continuum by successive diagonalizations of the molecular Hamiltonian with a slightly different parameter in the basis, like the size of the basis set (number of B-splines or partial waves) or, in our case, by changing the size of the electronic radial box. Since these resonances may appear just slightly above the ionization threshold, the radial box must be huge in order to obtain a large number of eigenvalues close to the threshold, i.e., to increase notoriously the density of states in the discretized lower continuum.

In the inset of Fig. 8, we show a typical stabilization energy diagram that shows the rapid variation of the continuum eigenenergies as a function of the UA box length $\tilde{r}_{\max} \in [1000, 10\,000]$ a.u. (with $\tilde{r}_{\max} = R\xi_{\max}/2$). However, at $E \sim 1.072 \times 10^{-5}$ a.u., the energy stabilizes indicating the presence of a discrete state (resonance) lying in the continuum at this energy. Following the procedure described in [34], one may obtain the density of states in the neighborhood of the resonance, which can be fitted to a Lorentz distribution to extract the energy position and width of the resonance. The internuclear distance for this calculation is $R = 0.01$ a.u., i.e., close to the UA limit. We have checked that the position and width obtained with the molecular code at this internuclear distance compares very well with the corresponding shape resonance that appears in screened H_2^+ (our results compare well with those obtained with our own one-electron atomic code based on Slater-type orbitals and with the results in [4]

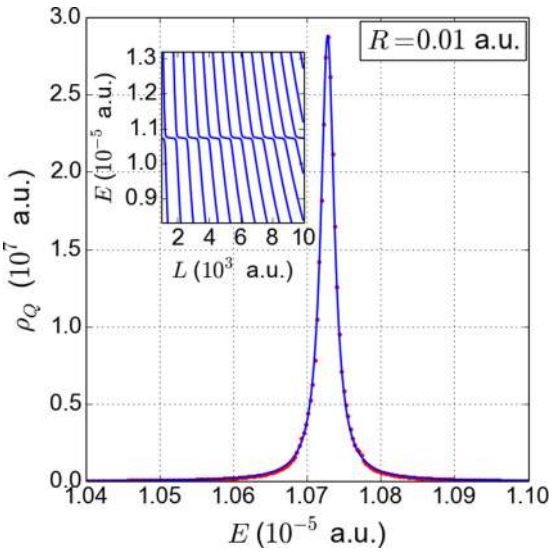

FIG. 8. Density of states $\rho_Q(E)$ associated to the lowest σ_g shape resonance lying in the electronic continuum slightly above the ionization threshold $E = 0$ of screened H_2^+ (screening parameter $\lambda = 0.080\,110\,64\bar{6}$ a.u., after [4]) close to the UA limit ($R = 0.01$ a.u.). The density is calculated from the energy stabilization diagram (see inset) as obtained from successive diagonalizations of the Hamiltonian by varying the UA box size $\tilde{r}_{\max} = R\xi_{\max}/2$ for the electron radial coordinate from 1000 to 10 000 a.u. Red dots: density extracted from the discretized energy grid. Blue line: fit of dots to a Lorentzian distribution.

for $\ell = 2$ and $\lambda = 0.080\,110\,64\bar{6}$ a.u.). We have followed the trend of the lowest σ_g, π_g, and δ_g shape resonances when the internuclear distance departs from the UA limit. In fact, the atomic resonance with $\ell = 2$ splits into three *gerade* molecular resonances (σ, π, and δ) since $0 \leqslant |m| \leqslant \ell$. Figure 9 shows that energies and widths for the σ_g and π_g resonances decrease with increasing R whereas the δ_g resonance state exhibits the opposite behavior. The trend of the resonance energies agrees with the typical behavior of bound states in unscreened H_2^+ close to the UA limit (in general, $nd\sigma_g$ and $nd\pi_g$ states stabilize for $R > 0$ and $nd\delta_g$ states increase their energies for $n \geqslant 3$). Nevertheless, the resonance energies considered in Fig. 9 are very close to the ionization threshold (where we must keep in mind that the application of the BO approximation is doubtful) and running stabilization calculations for larger internuclear distances is rather cumbersome, so that we cannot at this point follow the full R correlation of the atomic shape resonances (present unambiguously at $R = 0$, short R, and $R \to \infty$) to assess the survival of these structures at molecular equilibrium distances. Our conjecture is that some shape resonances such as σ_g and π_g merge into the lower continuum threshold and transform into Rydberg molecular states whereas others such as δ_g may survive all over the energy correlation diagram up to $R \to \infty$. Similarly, at large distances, some Rydberg states may again cross the upper ionization threshold to transform into atomic shape resonances.

The presence of such shape resonances at energies close to the ionization threshold and short internuclear distances deserves some analysis. In the unscreened two-center Coulomb problem, it is known that for very short internuclear distances

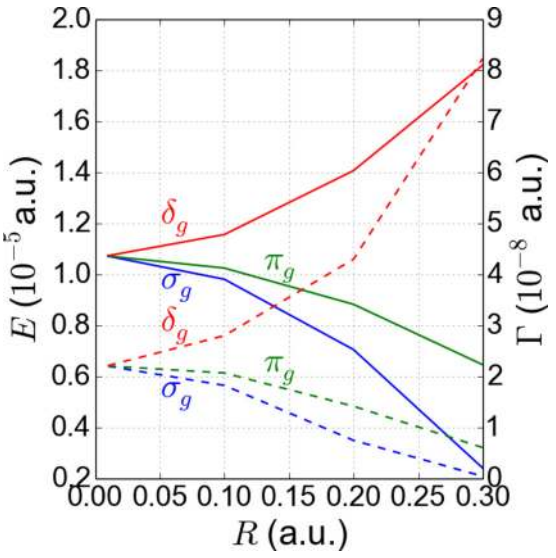

FIG. 9. Evolution of energies E (solid lines, energy scale on the left y axis) and widths Γ (dashed lines, energy scale on the right y axis) associated to the lowest σ_g (blue), π_g (green), and δ_g (red) shape resonances of screened H_2^+ (for screening parameter $\lambda = 0.080\,110\,64\bar{6}$ a.u.) as a function of the internuclear distance R in the region of the united atom (UA) limit.

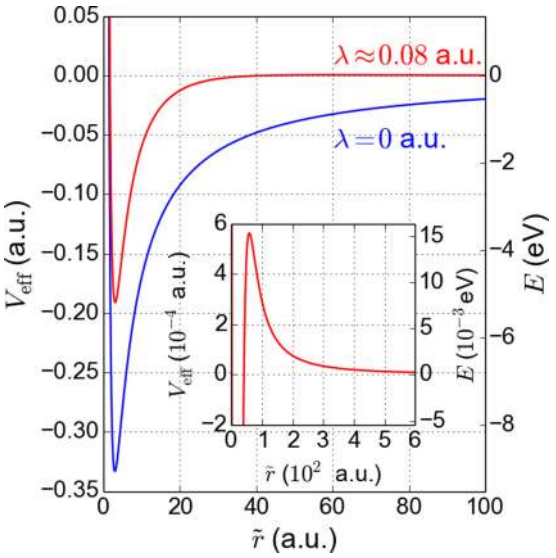

FIG. 10. Unscreened ($\lambda = 0$, blue) and screened ($\lambda = 0.080\,110\,64\bar{6}$ a.u., red) effective potentials [Eqs. (31) and (33), respectively] extracted from the outer ξ equation at short internuclear distances ($R = 0.3$ a.u.), low continuum energy, and a relatively small screening parameter λ (see text). The potentials are drawn in terms of the coordinate $\tilde{r} = R\xi/2$. Inset: detail of the potential barrier present in the screened case.

$\xi \to 2r/R \gg 1$ and $\eta \to \cos\theta$. In addition, for low energy $R^2E \ll 1$, and for homonuclear systems, $Z_1 = Z_2 = Z$, the inner angular equation for η simplifies to the differential equation for associated Legendre polynomials where the separation constant is simply $C = -\ell(\ell+1)$. Also, the outer radial equation for ξ can be transformed in an effective equation by taking $u(\xi) = \xi X(\xi)$ and letting $\xi^2 - 1 \sim \xi^2$, thus arriving to a Schrödinger equation

$$\left[-\frac{1}{2m_{\rm eff}}\frac{\partial^2}{\partial\xi^2} + V_{\rm eff}(\xi)\right]u(\xi) = Eu(\xi), \tag{30}$$

where $m_{\rm eff} = R^2/4$ and

$$V_{\rm eff}(\xi) = \frac{1}{2m_{\rm eff}}\left[\frac{m^2}{\xi^2(\xi^2-1)} + \frac{\ell(\ell+1)}{\xi^2}\right] - \frac{2Z}{R\xi/2}. \tag{31}$$

In the presence of screening, the potential for $Z_1 = Z_2 = Z$ can be also written as

$$\hat{V}(\xi,\eta) = -\frac{4Ze^{-\lambda\frac{R\xi}{2}}}{R(\xi^2-\eta^2)}\left[\xi\cosh\left(\lambda\frac{R}{2}\eta\right) + \eta\sinh\left(\lambda\frac{R}{2}\eta\right)\right]. \tag{32}$$

For small-R distances and/or small screening parameters, $\lambda\frac{R}{2} \ll 1$, and the potential can be expanded to the lowest order, leading to $V(\xi,\eta) = -\frac{4Z\xi e^{-\lambda\frac{R}{2}\xi}}{R(\xi^2-\eta^2)}$. This approximate potential keeps the outer (ξ) and the inner (η) equations separable in this approximation. Then, following the same steps that led us to Eq. (31) in the unscreened case, the outer equation for the ξ coordinate produces an analogous effective potential in the form

$$V_{\rm eff}(\xi) = \frac{1}{2m_{\rm eff}}\left[\frac{m^2}{\xi^2(\xi^2-1)} + \frac{\ell(\ell+1)}{\xi^2}\right] - \frac{2Ze^{-\lambda\frac{R}{2}\xi}}{R\xi/2}. \tag{33}$$

At variance with the effective potential in the unscreened case, the screened effective potential in (33) produces barrier potentials for $\ell > 0$. As an illustration, we plot both effective potentials (for $\lambda = 0$ and $\lambda \sim 0.08$ a.u.) in Fig. 10, as a function of the UA electronic coordinate $\tilde{r} = R\xi/2$, for an angular momentum $\ell = 2$ and a small internuclear distance $R = 0.3$ a.u. At first glance, the screening only modifies the range and depth of the binding potential, but a closer look at it (see the inset in Fig. 10) reveals that an extended but small potential barrier develops, which is responsible for the presence of shape resonances at low energies and short internuclear distances. This justifies that the molecular potential tends to produce the known shape resonances in the UA limit. However, their smooth continuity and survival at intermediate internuclear distances is yet unclear.

Quite differently, one may wonder how screened OEDMs promoted above the ionization threshold at given values of R (the $4f\sigma_u$ state at $R = 10$ a.u. in Fig. 3 is a prototypical example) transform when they merge into the molecular continuum as R decreases. This case is much more interesting because it deals with true molecular shape resonances at intermediate internuclear distances. Their presence, in principle, should not be surprising since these kinds of shape resonances already appear as special scattering states in single- and double-well potentials in one dimension [35]. To make a full characterization of this kind of molecular shape resonances in screened potentials is out of the scope of this work and we only show an illustration here. Figure 11 shows an energy correlation diagram (using a basis set with the *odd* partial waves $\ell = 1$, 3, 5, and 7) for the screened $3p\sigma_u$ and $4f\sigma_u$ states plus a set of continuum discretized states lying above $E = 0$ a.u. for $\lambda = 0.15$ a.u. It is clearly appreciated that the

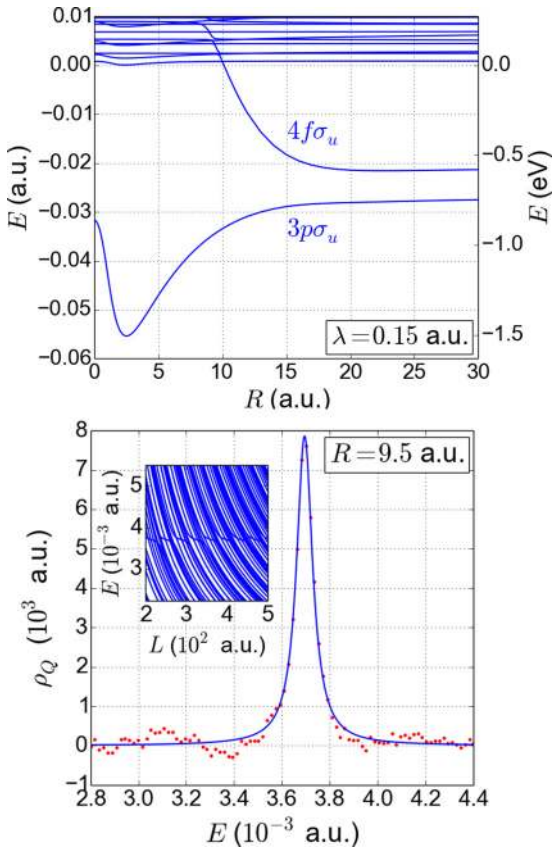

FIG. 11. (Top panel) Energy curves for the screened OEDM states $3p\sigma_u$ and $4f\sigma_u$ along with a discretized bunch of molecular continuum states above $E = 0$ a.u. The screening parameter $\lambda = 0.15$ a.u. is used. (Bottom panel) Density of states $\rho_Q(E)$ associated to the lowest $4f\sigma_u$ shape resonance lying in the electronic continuum slightly above the ionization threshold $E = 0$ a.u. of screened H_2^+ (screening parameter $\lambda = 0.15$ a.u.) at internuclear distance $R = 9.5$ a.u. The shape is calculated from the energy stabilization diagram (see inset), obtained from successive diagonalizations of the Hamiltonian by enlarging the box size $\tilde{r}_{\max} = R\xi_{\max}/2$ from 200 to 500 a.u. Red dots: density extracted from the discretized energy grid. Blue line: fit of dots to a Lorentzian distribution.

$4f\sigma_u$ state is electronically promoted to the continuum at $R = 10$ a.u. and then it is smoothly continued in the molecular continuum through a series of avoided crossings as R decreases to approach the UA limit. This is an indication of the survival of the state as a resonance in the continuum. In order to support this conclusion and to fully characterize this shape resonance, one may rely on methods to uncover resonances, at each fixed internuclear distance. To illustrate this point, we compute the position and width of the $4f\sigma_u$ resonance at $R = 9.5$ a.u. (where the state has already crossed the ionization threshold) using again the stabilization method. We obtain (similarly to Fig. 8) the energy stabilization diagram and the density of states ρ_Q, whose fit to a Lorentzian function yields $E_r = 0.0037$ a.u. and $\Gamma_r \sim 10^{-4}$ a.u. for $R = 9.5$ a.u. (see Fig. 11). As R gets shorter, the resonance energy is promoted to higher values and the width is expected to decrease. For screening values smaller than $\lambda = 0.15$ a.u., many other states in H_2^+ will show a similar behavior of *promotion to a shape resonance* as R decreases. In contrast, other screened states (notice $3s\sigma_g$ in Fig. 3) are promoted to the continuum as R increases, potentially transforming into another series of shape resonances.

IV. CONCLUSIONS

An efficient computational method for the calculation of electronic properties in one-electron diatomic molecules, where Coulomb interactions have been replaced by Yukawa-type interactions, has been described in detail. Laboratory and astrophysical weakly coupled plasmas exhibit screened Coulomb interactions that may affect the structure and dynamics of their molecular constituents; in this direction, our method may find useful applications. We have used a partial-wave expansion in terms of confocal elliptic coordinates and B-splines for the radial ξ coordinate, which are better suited for the computation of both molecular bound and continuum wave functions. Also, algorithms for the computation of dipole couplings for radiative dynamics and nonadiabatic radial couplings for collision dynamics are provided. The method of solution is very efficient and all computations run in a standard laptop computer within a few minutes.

Some illustrative results for molecular energies, wave functions, and their corresponding radiative dipole and nonadiabatic couplings for H_2^+ under screening are discussed. The calculation of these energies and dipole couplings are required elements to carry out calculations for the photoionization spectra. It is known that unscreened H_2^+ (unlike unscreened H) already presents Cooper-type minima in the photoabsorption cross section [36]. Similarly, multiphoton ionization of unscreened H_2^+ has been the subject of many recent studies using lasers (see, for instance, [37] with a discussion on Cooper minima). It will be of interest to understand the evolution of these zeros in the photoabsorption with increasing screening. Similarly, nonadiabatic couplings are essential to compute excitation and charge exchange cross sections in ion-atom collisions in Debye plasmas [38]. In addition, the introduction of other adjusted screening functions [12] in the potential may extend our method in order to obtain (screened) molecular orbitals in many-electron molecules.

We have also investigated the conditions for the presence of Borromean states in screened H_2^+ within the BO approximation, obtaining (in spite of the limitations of the BO approximation for its application with rather small electronic energies) an upper limit of screening in agreement with previous non-BO calculations. The presence of molecular shape resonances in screened H_2^+ is reported and analyzed, also in connection to already known atomic resonances in both the UA and SA limits. Beyond their intrinsic academic interest, its experimental detection could be of interest. Those resonances with u symmetry arising from the promotion to the continuum at short internuclear distances could in principle be detected in ultrafast photoionization experiments performed with *prepared* screened molecules in their ground state, by detecting low-energy resonance signals in the subsequent Yukawa nuclear explosion.

Finally, we have introduced a simple recipe for the solution of the arbitrary sign problem of variational eigenstates after diagonalization and a basic rule to assign the number of ξ-radial and η-angular nodes from their expansion coefficients.

ACKNOWLEDGMENTS

Work supported by the Advanced Grant of the European Research Council XCHEM 290853, the European COST Action XLIC CM1204, and the MINECO Project No. FIS2013-42002-R. A.F.O.-L. acknowledges financial support from EACEA through an Erasmus Mundus scholarship. J.L.S.-V. acknowledges financial support from Vicerrectoría de investigación at Universidad de Antioquia (Contract No. E01538 and Estrategia de Sostenibilidad 2016-2017) and from Departamento Administrativo de Ciencia, Tecnología e Innovación (COLCIENCIAS, Colombia) under Contract No. 111565842968.

APPENDIX A: ARBITRARY SIGN IN THE WAVE FUNCTIONS

It is well known that eigenfunctions obtained from the diagonalization of the Hamiltonian (projected on a basis set of real functions) have an arbitrary phase, so that the sign of the (real) eigenstate is randomly $+1$ or -1. For atoms this is mostly irrelevant but for molecules, eigenfunctions for different values of the nuclear geometry are obtained by diagonalizing the Hamiltonian at different internuclear distances R and sometimes by using a slightly different basis set at each geometry. Each separate R diagonalization eventually may bring a different phase for the same molecular state. This has no consequences on the energies but it may cause sudden jumps in the matrix elements $\langle\Psi_n|\hat{O}|\Psi_{n'}\rangle$ as a function of the internuclear distance R. These matrix elements should therefore be corrected to reflect the smooth R behavior that would arise if all states were obtained by using a consistent phase for all R. This is usually known as the *arbitrary sign problem*, which has no general formal solution, although some practical prescriptions have been implemented. Since in this work we obtain dipolar matrix elements and nonadiabatic radial couplings between electronic eigenstates of H_2^+ coming from a diagonalization in a basis (note that this is at variance with the exact eigenstates of unscreened H_2^+ for which this sign problem is absent), we outline here two procedures to circumvent this problem, at least in H_2^+, for which we have implemented them successfully.

1. Retarded overlap method

Instead of correcting the matrix elements $\langle\Psi_n|\hat{O}|\Psi_{n'}\rangle$, we would like to fix the phases for the two contributing wave functions $\{\Psi_n(\mathbf{r};R),\Psi_{n'}(\mathbf{r};R)\}$ along R. A way to do it is to preserve always the same phase, starting from an initial reference value at a short R distance, by computing the overlap integral between the same wave function at two close values of R (see, for instance, [39,40]), i.e.,

$$S_n(R,R+\Delta R)=\int d\mathbf{r}\,\Psi_n(\mathbf{r};R)\Psi_n(\mathbf{r};R+\Delta R). \quad \text{(A1)}$$

This retarded overlap matrix should give ±1, provided ΔR is sufficiently small: if $S_n\sim+1$ the phase has not changed, if $S_n\sim-1$ the phase has changed from R to $R+\Delta R$ and then we proceed to amend this change of phase.

In order to compute this retarded overlap integral with the same wave function but at different values of R, we proceed as follows, considering our expansion in confocal elliptic coordinates. We have the wave functions obtained from diagonalizations at R and R',

$$\psi^m(\xi,\eta,\phi;R)=\sum_{\ell=|m|}^{\ell_{\max}}\Phi_\ell^m(\xi)\Theta_\ell^m(\eta)\frac{e^{im\phi}}{\sqrt{2\pi}},\quad m\geqslant 0 \quad \text{(A2)}$$

and

$$\psi^m(\xi',\eta',\phi;R')=\sum_{\ell=|m|}^{\ell_{\max}}\Phi_\ell^m(\xi')\Theta_\ell^m(\eta')\frac{e^{im\phi}}{\sqrt{2\pi}},\quad m\geqslant 0 \quad \text{(A3)}$$

with $\{\xi=(r_1+r_2)/R,\ \eta=(r_1-r_2)/R\}$ and $\{\xi'=(r_1'+r_2')/R',\ \eta'=(r_1'-r_2')/R'\}$ being the confocal elliptic coordinates at R and R', respectively. Thus, the overlap integral can be calculated as (we assume the Jacobian volume element to be taken at R with $\{\xi,\eta,\phi\}$ coordinates)

$$S=\sum_{\ell,\ell'=|m|}^{\ell_{\max}}\frac{R^3}{8}\int d\xi\,d\eta\,d\phi(\xi^2-\eta^2)\times\Phi_\ell^m(\xi)\Theta_\ell^m(\eta)\frac{e^{-im\phi}}{\sqrt{2\pi}}\Phi_{\ell'}^m(\xi')\Theta_{\ell'}^m(\eta')\frac{e^{im\phi}}{\sqrt{2\pi}}. \quad \text{(A4)}$$

To perform this integral we can transform the coordinates (ξ',η') in terms of (ξ,η) provided that they represent the same point in coordinate space for the electron, i.e., $(x,y,z)=(x',y',z')$, according to the formulas

$$\xi'(\xi,\eta)=\frac{r_1(\xi,\eta)+r_2(\xi,\eta)}{R'},\quad \eta'(\xi,\eta)=\frac{r_1(\xi,\eta)-r_2(\xi,\eta)}{R'}, \quad \text{(A5)}$$

where $r_{1,2}(\xi,\eta)$ can be obtained from Eq. (4). This retarded overlap method works fine in all our applications, provided that ΔR is not too large.

2. Projection onto a reference vector

Here, we refer to a very simple way to fix the phase of a given eigenvector, using a reference vector in the Hilbert space. For simplicity, let us assume two vectors $\{\mathbf{v},\mathbf{r}\}\in\mathbb{R}^3$, where $\mathbf{v}=v_x\hat{i}+v_y\hat{j}+v_z\hat{k}$ plays the role of our eigenvector obtained from diagonalization and $\mathbf{r}$ is a reference vector chosen at convenience, for instance, $\mathbf{r}=\hat{i}+\hat{j}+\hat{k}$. The scalar product gives the projection of the eigenvector $\mathbf{v}$ over the reference vector $\mathbf{r}$, i.e., $\mathbf{v}\cdot\mathbf{r}=v_x+v_y+v_z$, a scalar whose sign can be fixed once and for all; for example, the projection of the eigenvector over the reference vector must be always positive. Note that this choice of reference vector implies to simply check the sign of the sum of the expansion coefficients of the eigenvector.

In the general case of using a nonorthogonal basis $\{\mathbf{u}_i\}_{i=1}^N$ for the expansions with overlap matrix $\mathbf{S}$, the scalar product reads as

$$\mathbf{v}\cdot\mathbf{r}=\sum_i v_i\mathbf{u}_i\cdot\sum_j r_j\mathbf{u}_j=\sum_{i,j}v_iS_{ij}r_j.$$

If, once again, we choose $r_j=1\ \forall\ j$, this projection implies the evaluation $\mathbf{v}\cdot\mathbf{r}=\sum_i(\mathbf{S}\cdot\mathbf{v})_i$. In some occasions the chosen

basis (like B-splines in our case), although nonorthogonal, only contains positive-definite functions with minimal support and thus it has an overlap matrix whose structure is diagonally banded. In this case, it happens to occur that $\sum_i (\mathbf{S}\cdot\mathbf{v})_i$ provides the same projection sign than the more simple operation $\sum_i v_i$. In fact, this is what we find with our diagonalized OEDM wave functions expanded in terms of B-splines: *the sum of the expansion coefficients* $\sum_{i,\ell} c_{i\ell}^m$ *in Eq. (6) provides the quasiprojection onto a reference vector*, and we keep the positive sign for this projection for the same eigenvector along the R-correlation diagram from $R = 0.1$ up to $R = 100$ a.u. We find that this simple projection method also works fine for our (screened or unscreened) OEDMs and it always provides the same sign correction as the retarded overlap method but at a much lower computational cost.

The extension of this method to more general cases should be taken with caution since we have learned that our OEDM eigenvector does smoothly rotate in the Hilbert space for increasing internuclear distances, and the rotation angle of the eigenstate in the R interval [0.1,100] a.u. is always under $\pi/2$ rad, which reduces the ambiguity in the projection procedure and the sign choice with respect to the direction of the reference vector. However, for faster rotations with the nuclear geometry, the method could be implemented piecewise updating the reference vector for consecutive segments in the geometry. In general, this issue should be analyzed for each particular case (in terms of the basis used both in the one-electron and the many-electron problem). To our knowledge, this extremely simple procedure has not been discussed previously.

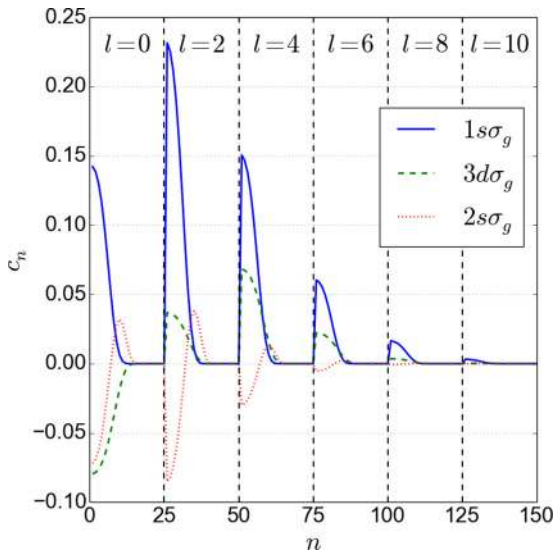

FIG. 12. Expansion coefficients $c_n \equiv c_{i\ell}^{m=0}$ of the unscreened H_2^+ wave function in Eq. (6) for the three lowest $k\sigma_g$ states [$k = 1$, 2, and 3 which correspond to the $1s\sigma_g$ (blue solid line), $3d\sigma_g$ (green dashed line), and $2s\sigma_g$ (red dotted line) labels in the UA limit] at the internuclear distance $R = 20$ a.u. Vertical dashed lines separate blocks corresponding to different angular momenta in the partial-wave expansion from $\ell = 0$ to 10. Each ℓ block contains coefficients corresponding to the radial ξ expansion in terms of $N_\xi = 25$ B-splines, i.e., $i = 1, \ldots, 25$. The index n then runs within each ℓ block from $\frac{\ell}{2}N_\xi + 1$ to $(\frac{\ell}{2}+1)N_\xi$.

APPENDIX B: ANGULAR AND RADIAL NODES OF UNSCREENED WAVE FUNCTIONS

For any given unscreened OEDM wave function, obtained from diagonalization of the electronic Hamiltonian using the variational expansion given in Eq. (6), one may extract the number of radial n_ξ and angular n_η nodes either by (i) a trivial simple inspection of the wave function plotted in the plane (ξ, η) for a given internuclear distance R or (ii) by simply analyzing the expansion coefficients $c_{i\ell}^m$. Needless to say, the second approach does not require the evaluation of the wave function on a grid.

Here, we explain the second procedure. For instance, in Fig. 12, we plot the expansion coefficients $c_{i\ell}^0$ for the lowest unscreened OEDM states of symmetry σ_g at $R = 20$ a.u. (i.e., $1s\sigma_g$, $3d\sigma_g$, and $2s\sigma_g$, although in rigor they must be named $1\sigma_g$,$2\sigma_g$, and $3\sigma_g$, respectively) which [from inspection of the contour plot of the wave function in the (ξ,η) plane] are known to have radial and angular nodes $(n_\xi,n_\eta,n_\phi) = (0,0,0)$, $(0,2,0)$, and $(1,0,0)$, respectively. For the $1s\sigma_g$ state, mostly five *even*

TABLE I. Values of the nodal numbers n_ξ, n_η, and n_ϕ associated to the confocal elliptic coordinates ξ, η, and ϕ, with n_ξ and N_c obtained from direct inspection of plots of the expansion coefficients $c_{i\ell}^m$ and with the application of expression (B1) (in all cases quoted here $n_o = 0$). The nodes correspond to the lowest unscreened OEDMs states for symmetries $\sigma_{g/u}$, $\pi_{g/u}$, and $\delta_{g/u}$, evaluated at the internuclear distance $R = 20$ a.u. and they are listed, using the UA nomenclature for OEDMs, according to the energy ordering at this internuclear distance.

	Nodes			Eq. (B1)	
State	n_ξ	n_η	n_ϕ	N_c	s
$1s\sigma_g$	0	0	0	0	0
$3d\sigma_g$	0	2	0	1	0
$2s\sigma_g$	1	0	0	0	0
$5g\sigma_g$	0	4	0	2	0
$4d\sigma_g$	1	2	0	1	0
$3s\sigma_g$	2	0	0	0	0
$2p\sigma_u$	0	1	0	0	1
$4f\sigma_u$	0	3	0	1	1
$3p\sigma_u$	1	1	0	0	1
$5f\sigma_u$	1	3	0	1	1
$4p\sigma_u$	2	1	0	0	1
$6h\sigma_u$	0	5	0	2	1
$3d\pi_g$	0	1	1	0	1
$5g\pi_g$	0	3	1	1	1
$4d\pi_g$	1	1	1	0	1
$6g\pi_g$	1	3	1	1	1
$2p\pi_u$	0	0	1	0	0
$4f\pi_u$	0	2	1	1	0
$3p\pi_u$	1	0	1	0	0
$5f\pi_u$	1	2	1	1	0
$3d\delta_g$	0	0	2	0	0
$5g\delta_g$	0	2	2	1	0
$4d\delta_g$	1	0	2	0	0
$4f\delta_u$	0	1	2	0	1
$5f\delta_u$	1	1	2	0	1
$6h\delta_u$	0	3	2	1	1

partial waves ($\ell = 0$, 2, 4, 6, and 8) participate significantly and the $\ell = 2$ contribution dominates whereas for the $3d\sigma_g$ state, the partial waves $\ell = 0$ and 4 contribute more than $\ell = 2$. It is worth stressing that for $1s\sigma_g$ all ℓ blocks have the same sign (positive). Similarly, for $2s\sigma_g$ the leading coefficients within all ℓ blocks have also the same sign (negative). At variance, for $3d\sigma_g$ there is a global change of sign from block $\ell = 0$ (negative) to block $\ell = 2$ (positive) and only this change along all ℓ blocks. We call N_c this number of global sign changes for ℓ blocks along the set of expansion coefficients. We find that the number of angular nodes n_η for any state (independently of its excitation) is given by

$$n_\eta = 2(N_c + n_o) + s, \tag{B1}$$

where N_c is the number of ℓ-block sign inversions, n_o is the number of null ℓ blocks before the first nonzero ℓ block (especially for highly lying states), and $s = 0$ for even (odd) $|m|$ and *gerade (ungerade)* symmetry ($\sigma_g, \pi_u, \delta_g, \ldots$) or $s = 1$ for even (odd) $|m|$ and *ungerade (gerade)* symmetry (σ_u, π_g, $\delta_u, \ldots$). Additionally, the number of radial nodes n_ξ is simply given by the number of nodes the coefficients *curve* c_n has within each ℓ block, the latter rule due to the minimal support property of B-splines. Accordingly, Fig. 12 indicates that $1s\sigma_g$ and $3d\sigma_g$ have no radial nodes and $2s\sigma_g$ has one radial node. A simple inspection of this kind of plot for the expansion coefficients allows us to fully determine and classify states coming from diagonalization according to their number of nodes, as shown in Table I for the lowest states in the symmetries $\sigma_{g/u}$, $\pi_{g/u}$, and $\delta_{g/u}$. Mind that the sum of the expansion coefficients in Appendix A was used to fix the phase of the state along the energy correlation diagram from UA to SA limits.

To fully understand these simple rules and to find a corresponding proof is beyond the scope of this work, but we believe that this is a property associated to the fact that we are using (i) positive-definite basis functions (B-splines) for the ξ coordinate, (ii) orthogonal polynomials for the η expansion (associated Legendre polynomials), which may relate these considerations with the fulfillment of a generalized Descartes' rule for orthogonal polynomials. The well-known Descartes' rule of signs for polynomials states that "*. . . if the terms of a single-variable polynomial with real coefficients are ordered by descending variable exponent, then the number of positive roots of the polynomial is either equal to the number of sign differences between consecutive nonzero coefficients, or is less than it by an even number*." Thus, the number of sign changes between consecutive coefficients is related to the number of nodes. The analogy in our case must be understood for the coefficients accompanying each associated Legendre polynomial in the partial-wave expansion (6), for a given angular momentum (which is the sum within each ℓ block, i.e., $C_\ell = \sum_i^{N_\xi} c_{i\ell}^m$). Of course, the original Descartes' rule is based on the nonorthogonal basis set of monomials $\{x^n\}_n$ but a generalization of the rule for general orthogonal polynomials is feasible after the seminal works of Marden [41] and Obreshkoff (see [42]), so that this connection cannot be disregarded.

[1] P. Debye and E. Hückel, Physikalische Zeitschrift **24**, 185 (1923).
[2] S. Ichimaru, *Plasma Physics: An Introduction to Statistical Physics of Charged Particles* (Benjamin Cummings, Menlo Park, 1986).
[3] R. Janev, S. B. Zhang, and J. Wang, Matter Radiat. Extremes **1**, 237 (2016).
[4] M. Bylicki, A. Stachów, J. Karwowski, and P. K. Mukherjee, Chem. Phys. **331**, 346 (2007).
[5] P. K. Mukherjee, S. Fritzsche, and B. Fricke, Phys. Lett. A **360**, 287 (2006).
[6] S. Kar and Y. K. Ho, Phys. Lett. A **368**, 476 (2007).
[7] A. Ghoshal and Y. K. Ho, Int. J. Quantum Chem. **111**, 4288 (2011).
[8] S. Kar and Y. K. Ho, Chem. Phys. Lett. **506**, 282 (2011).
[9] S. Kar and Y. K. Ho, Phys. Rev. A **86**, 014502 (2012).
[10] L. Bertini, M. Mella, D. Bressanini, and G. Morosi, Phys. Rev. A **69**, 042504 (2004).
[11] J. M. Ugalde, C. Sarasola, and X. Lopez, Phys. Rev. A **56**, 1642 (1997).
[12] U. Wille and R. Hippler, Phys. Rep. **132**, 129 (1986).
[13] B. Bransden and M. R. C. McDowell, *Charge Exchange and the Theory of Ion-Atom Collisions* (Clarendon, Oxford, 1992).
[14] A. Macías and A. Riera, Phys. Rep. **90**, 299 (1982).
[15] Ø. Burrau, Kgl. Danske Videnskab. Selskab. Mat. Fys. Medd. **7**, No. 14 (1927).
[16] E. Teller, Z. Phys. **61**, 458 (1930).
[17] E. A. Hylleraas, Z. Phys. **71**, 739 (1931).
[18] G. Jaffé, Z. Phys. **87**, 535 (1934).
[19] J. M. Peek, J. Chem. Phys. **43**, 3004 (1965).
[20] G. Hunter and H. Pritchard, J. Chem. Phys. **46**, 2146 (1967).
[21] J. Power, Philos. Trans. R. Soc. **274**, 663 (1973).
[22] P. Greenland, Phys. Rep. **81**, 131 (1982).
[23] J. Rost, J. Briggs, and P. Greenland, J. Phys. B: At., Mol. Opt. Phys. **22**, L353 (1989).
[24] C. Coulson and A. Joseph, Int. J. Quantum Chem. **1**, 337 (1967).
[25] C. de Boor, *A Practical Guide to Splines* (Springer, New York, 1978).
[26] H. Bachau, E. Cormier, P. Decleva, J. E. Hansen, and F. Martín, Rep. Prog. Phys. **64**, 1815 (2001).
[27] M. Barat and W. Lichten, Phys. Rev. A **6**, 211 (1972).
[28] H. Lefebvre-Brion and R. W. Field, *The Spectra and Dynamics of Diatomic Molecules* (Elsevier, Amsterdam, 2004).
[29] R. Schinke and H. Krüger, J. Chem. Phys. **64**, 2450 (1976).
[30] A. Salin, Comput. Phys. Commun. **14**, 121 (1978).
[31] T. G. Winter and N. F. Lane, Phys. Rev. A **17**, 66 (1978).
[32] M. Kimura and N. Lane, Adv. At. Mol. Opt. Phys. **26**, 79 (1990).
[33] Y. Wu, J. Wang, P. Krstic, and R. Janev, J. Phys. B: At., Mol. Opt. Phys. **43**, 201003 (2010).
[34] V. A. Mandelshtam, T. R. Ravuri, and H. S. Taylor, Phys. Rev. Lett. **70**, 1932 (1993).
[35] F. Schwabl, *Quantum Mechanics* (Springer, Heidelberg, 1995).

[36] R. Della Picca, P. D. Fainstein, M. L. Martiarena, and A. Dubois, Phys. Rev. A **77**, 022702 (2008).
[37] X. Guan, E. B. Secor, K. Bartschat, and B. I. Schneider, Phys. Rev. A **84**, 033420 (2011).
[38] Y. Zhang, C. H. Liu, Y. Wu, J. G. Wang, Y. Z. Qu, and J. Yan, Phys. Rev. A **82**, 052706 (2010).
[39] L. F. Errea, L. Fernández, A. Macías, L. Méndez, I. Rabadán, and A. Riera, J. Chem. Phys. **121**, 1663 (2004).
[40] V. Mezoui Ndo, L. O. Owono, B. Piraux, S. Barmaki, M. Førre, and H. Bachau, Phys. Rev. A **86**, 013416 (2012).
[41] M. Marden, Ann. Math. **33**, 118 (1932).
[42] A. M. Ostrowski, J. Math. Mech. **14**, 195 (1965).